

Free-breathing and ungated cardiac cine using navigator-less spiral SToRM

*Abdul Haseeb Ahmed**, *Yasir Mohsin**, *Ruixi Zhou†*, *Yang Yang***, *Michael Salerno†*, *Prashant Nagpal‡*, *Mathews Jacob**

** Department of Electrical and Computer Engineering, The University of Iowa, Iowa City, IA*

‡ Department of Radiology, The University of Iowa, Iowa City, IA

† Department of Biomedical Engineering, University of Virginia, Charlottesville, VA

*** Department of Medicine, University of Virginia, Charlottesville, VA*

April 25, 2022

Correspondence to: Mathews Jacob

The University of Iowa

Department of Electrical and Computer Engineering

4016 Seamans Center

Iowa City, IA 52242

Email: mathews-jacob@uiowa.edu

arXiv:1901.05542v1 [eess.IV] 16 Jan 2019

Abstract

Purpose: To develop a free-breathing and ungated cardiac MRI scheme using an iterative kernel low-rank algorithm and self-gated spiral sequence.

Methods: The data were acquired continuously over 8-16 seconds per slice without ECG gating or breath holding using a golden-angle gradient echo spiral sequence. The reconstruction scheme relies on the manifold structure of a dynamic data to recover it from the highly undersampled measurements. An iterative kernel low-rank algorithm is introduced to estimate the manifold structure of the images, or equivalently the manifold Laplacian matrix, from the central k-space regions. The iterative algorithm, coupled with the non-Cartesian acquisitions, eliminates the need for dedicated navigators to estimate the manifold Laplacian, unlike previous manifold methods, thus improving sampling efficiency.

Results: The proposed method is demonstrated in patients with different breathing patterns and cardiac rates. The experiments show the ability of our proposed iterative strategy to reduce spatial and temporal blurring compared to state-of-the-art methods.

Conclusion: The iterative STORM algorithm facilitates the extension of manifold regularization to navigator-less spiral acquisitions, thus improving sampling efficiency. The proposed scheme eliminates the need for breath-holding and ECG gating, while facilitating the imaging of the cardiac function in different respiratory phases.

Keywords: cardiac reconstruction, free-breathing, kernel methods, manifold models, non-ECG gated, cardiac MRI

INTRODUCTION

Breath-held cine MRI is an integral part of clinical cardiac exams and is widely used for the anatomical and functional assessment of the heart. Diagnostic cine images require breath holding to achieve high spatial and temporal resolution, which is often challenging for the children and the patients with heart failure, chronic obstructive pulmonary disease (COPD), or obesity (1). In addition, multiple breath-holds along with intermittent pauses for recovery from breath-holds also prolong the scan time, adversely impacting patient comfort and compliance. The scans from different slices may also suffer from inconsistencies between breath-held positions. The acceleration of cardiac cine MRI has witnessed extensive research. Classical approaches include parallel MRI, where the diversity of coil sensitivities are exploited to reduce the breath-hold duration. Recent approaches further improve the performance by additionally exploiting the structure of k - f space (2–4), sparsity (5, 6), low-rank property (7–10), learned dictionaries (11, 12), motion-compensated methods (13–15), and kernel low-rank methods (16). When the subjects cannot hold their breath, a standard alternative is real-time imaging that does not require breath holding or ECG gating. However, these approaches have been shown to sacrifice spatial and/or temporal resolution (17–19). Another approach is the use of diaphragmatic navigators, which restricts the acquisition to images in the specific respiratory phase (20–22). However, the drawbacks of these schemes are low respiratory gating efficiency and variability in the scan time due to respiratory patterns. Several groups of methods that rely on radial acquisitions were introduced in the recent years, which estimate the cardiac and respiratory phases from the central k -space regions using band-pass filtering. These methods usually require careful selection of receive coil elements to obtain self-gating signals since each coil has different sensitivity to cardiac motion and respiratory motion. The data is then binned to the respective phases, followed by reconstruction using compressed sensing (23, 24) or low-rank tensor methods (25). Methods that rely on respiratory motion compensation, followed by binning have also been introduced to improve computational efficiency (26, 27). A challenge with these approaches is the dependency on the phase estimation using band-pass filtering that relies on cardiac and respiratory rates, which may degrade in the presence of irregular respiratory motion or arrhythmia. In addition, since they rely on the explicit segmentation of the data into respective phases, the applicability of these schemes to cases with arrhythmia (28) or non-cardiac applications (e.g. speech) is not straightforward.

We had recently introduced the smoothness regularization on manifold (SToRM) approach, which enables ungated cardiac cine imaging in the free breathing mode using radial acquisitions (29–31). The SToRM

algorithm assumes that the images in free breathing dataset lie on a smooth and low-dimensional manifold, parameterized by a few variables (e.g. cardiac & respiratory phases). The manifold regularization prior facilitates the implicit sharing of data between images in the dataset that have similar cardiac or respiratory phases, which is an alternative to explicit motion-resolved strategies (23–25). This acquisition scheme relies on the navigator radial spokes, which are used to compute the graph Laplacian matrix that captures the structure of the manifold, or equivalently the similarity between images in the dataset. An off-diagonal entry of the Laplacian matrix is high if the corresponding pair of frames have similar cardiac and respiratory phases, even though they may be well-separated in time. This implicit soft-binning strategy offers the potential to simultaneously image cardiac and respiratory function, and it eliminates the need for explicit binning of data as mentioned in (23–25). Since the framework does not require the associated complex processing steps that assume the periodicity of the cardiac/respiratory motion, it is readily applicable to several dynamic applications, including speech imaging as shown in (29), and cardiac applications involving arrhythmia. We had recently introduced a kernel low-rank algorithm to further improve the estimation of the manifold Laplacian matrix from noisy navigator measurements, which resulted in higher robustness to noise and subtle patient motion (31, 32). A challenge with the navigator-based radial acquisition scheme in (29) is the relatively lower sampling efficiency, resulting from the time to acquire multiple navigator spokes per image. In addition, more efficient variable-density non-Cartesian sampling trajectories may be used to further improve the performance of the STORM framework.

In this work, we introduce a navigator-free STORM algorithm for the recovery of free breathing and ungated cardiac MRI data from a variable-density spiral gradient echo (GRE) acquisition. The GRE acquisition is free from banding artifacts and does not require additional frequency scouts. In comparison to navigated radial acquisition scheme in (29), the spiral acquisition scheme offers higher sampling efficiency and signal-to-noise ratio. In addition, we propose to exploit the central k-space regions that are relatively more highly sampled than in the radial settings and thus eliminate the need for navigator-based acquisition to determine the Laplacian matrix. We propose to recover the images from undersampled measurements using the iterative kernel low-rank algorithm (31, 32). Specifically, we model the images as high-dimensional points on a smooth manifold, which is represented as the zero level-set of a bandlimited function. We have shown that the non-linear features of such images form a low-rank matrix (31). We propose to recover the images from their undersampled multi-channel spiral measurements using an iterative low-rank minimization algorithm. This algorithm was only demonstrated in the fully sampled denoising setting in the past

(31, 32); the extension of this algorithm to the undersampled setting is one of the main contributions of this work. The main difference of the proposed algorithm with past kernel low-rank methods (33) is that we do not require the explicit evaluation of the feature maps of the images. Our proposed algorithm relies on the kernel trick, which makes it applicable to kernel low-rank modeling of images; we note that (33) exploited the kernel low-rank structure of small signals such as voxel intensity profiles, which made the explicit evaluation of the non-linear maps feasible. Furthermore, the recovery of large number of frames from their highly undersampled measurements considered in this work is not ideally suited to their setting, as stated in their work (33). To improve the computational efficiency of the algorithm, we rely on a two-step strategy. Specifically, we recover low-resolution image frames from the central k-space regions that are relatively better sampled using the kernel low-rank algorithm. Note that the central k-space regions are still heavily undersampled. The kernel low-rank penalty makes the recovery from undersampled measurements well-posed, providing alias-free reconstructions. More importantly, it provides the Laplacian matrix of the manifold as a by-product. The small size of the images translates to a fast recovery. We propose to recover the high-resolution images by solving a simple quadratic optimization problem. Note that this scheme is similar to the classical STORM scheme (29), with the exception that the Laplacian is obtained from central k-space regions using an iterative kernel low-rank minimization rather than using exponential kernel from navigators. To further improve computational efficiency, we approximate the Laplacian matrix using few of its lower eigenvectors. Since the number of basis functions is an order of magnitude smaller than the number of images in the dataset, this approach reduces the computational complexity and memory demand by an order of magnitude. We validate the proposed method on simulated and in vivo datasets on short axis view. We also compare the results with existing reconstruction techniques including low-rank regularization (34) and XD-GRASP (24).

METHODS

Overview of STORM framework (29)

The STORM framework relies on the manifold structure of images in the real-time cardiac MRI dataset to perform implicit motion-resolved recovery of the data, which is an alternative to explicit binning-based strategies (23–25); the images are modeled as points on a low-dimensional manifold, embedded in a high-dimensional Euclidean space, whose dimension is equal to the number of pixels in the image. The dimension

of manifold depends on the degrees of freedom, which are cardiac and respiratory phases in case of free breathing, ungated cardiac MRI. The STORM scheme uses a smoothness prior on the manifold of images:

$$\int_{\mathcal{M}} \|\nabla x\|^2 \approx \frac{1}{2} \sum_{i,j=1}^k \mathbf{W}_{i,j} \|\mathbf{x}_i - \mathbf{x}_j\|^2 = \text{trace}(\mathbf{X} \mathbf{L} \mathbf{X}^H). \quad [1]$$

The weights $\mathbf{W}_{i,j}$ which specify the neighborhood structure on the manifold were estimated from radial navigator acquisitions of each frame specified by \mathbf{z}_i as

$$\mathbf{W}_{ij} = e^{-\frac{\|\mathbf{z}_i - \mathbf{z}_j\|^2}{\sigma^2}} \quad [2]$$

The use of the exponential kernel assigns higher weights to image pairs \mathbf{x}_i and \mathbf{x}_j , if they are local neighbors on the manifold. Here, \mathbf{X} is the Casorati matrix, whose columns correspond to $\mathbf{x}_i; i = 1, \dots, k$. $\mathbf{L} = \mathbf{D} - \mathbf{W}$ is the graph Laplacian, which approximates the Laplace Beltrami operator. \mathbf{D} is a diagonal matrix with elements defined as $\mathbf{D}_{ii} = \sum_j \mathbf{W}_{ij}$. STORM performs the joint recovery of the images in the dataset by solving the following problem:

$$\mathbf{X}^* = \arg \min_{\mathbf{X}} \|\mathcal{A}(\mathbf{X}) - \mathbf{B}\|_F^2 + \lambda \text{trace}(\mathbf{X} \mathbf{L} \mathbf{X}^H) \quad [3]$$

Where \mathcal{A} is the measurement operator that account multichannel spiral sampling of the columns of \mathbf{X} , which are the image frames.

The direct use of the weight estimation scheme [2] often results in oversmoothing of the images. Hence, it is a general practice in graph Laplacian regularization to only retain the most important N neighbors for each node and set the other weights to zero; this construction constrains the manifold to be a regular graph. Unfortunately, the approximation of an irregularly sampled manifold by a regular graph often results in a trade-off between an oversmoothing of poorly sampled manifold neighborhoods and a good recovery of well sampled neighborhoods.

Laplacian estimation for navigator-less spiral data

The STORM approach of estimating the weights as in [2] cannot be readily applied to our setting since the acquisition scheme does not involve navigators. Inspired by our recent work (31, 32), we propose to

recover the data using kernel low-rank regularization. Specifically, we model the images $\mathbf{x}_1, \dots, \mathbf{x}_N$ as high-dimensional points on a smooth manifold/surface. We assume that the manifold / surface is the zero levelset (35) of a bandlimited function. We have shown that under this assumption, the exponential feature maps of the images denoted by

$$\Phi(\mathbf{X}) = \begin{bmatrix} \phi(\mathbf{x}_1) & \phi(\mathbf{x}_2) & \dots & \phi(\mathbf{x}_N) \end{bmatrix} \quad [4]$$

form a low-rank matrix (31, 32). Here, the exponential maps ϕ are specified by

$$\phi(\mathbf{x}) = \begin{bmatrix} \frac{1}{\sigma^2 \|\mathbf{k}\|} \exp(j\mathbf{k}_1^T \mathbf{x}) \\ \vdots \\ \frac{1}{\sigma^2 \|\mathbf{k}\|} \exp(j\mathbf{k}_P^T \mathbf{x}) \end{bmatrix} \quad [5]$$

where $\mathbf{k}_1, \dots, \mathbf{k}_P$ are points on a discrete Lattice; see (31, 32) for details. We propose to recover the images $\mathbf{x}_1, \dots, \mathbf{x}_N$ from their undersampled measurements using kernel low-rank regularization:

$$\mathbf{X}^* = \arg \min_{\mathbf{X}} \|\mathcal{A}(\mathbf{X}) - \mathbf{B}\|_F^2 + \lambda_1 \|\Phi(\mathbf{X})\|_* + \lambda_2 \underbrace{\sum_i \|\mathbf{x}_{(i+1)} - \mathbf{x}_i\|^2}_{\text{trace}(\mathbf{X}\mathbf{L}_n\mathbf{X}^H)} \quad [6]$$

where $\|\cdot\|_*$ denotes the nuclear norm. The second term in [6] is the nuclear norm of the non-linear features of the images \mathbf{x}_i , which promotes the low-rank nature of $\Phi(\mathbf{X})$, or equivalently encourages the images to lie on smooth surfaces/manifolds. Note that this is a non-linear generalization to classical low-rank/subspace models (9, 34), which are widely used in dynamic imaging. The last term in [6] is a classical temporal Tikhonov regularization prior to encourage the similarity of each image in the dataset with its immediate neighbors. λ_2 is chosen as a small value to minimize abrupt jumps in the time profile. This term exploits the prior information that the image frames in the time series change slowly as a function of time, which the manifold based non-local prior is not capable of exploiting. Note that the Tikhonov prior can be rewritten as $\text{trace}(\mathbf{X}\mathbf{L}_n\mathbf{X}^H)$, where \mathbf{L}_n is the matrix with block diagonal matrix with block diagonal entries as $[1, -2, 1]$. If the images $\mathbf{x}_1, \dots, \mathbf{x}_N$ lie on a smooth surface in high dimensional space, then the matrix $\Phi(\mathbf{X})$ is heavily low-rank (31, 32). Note that this is a non-linear generalization of low-rank methods (9, 34) that are widely used in dynamic imaging applications.

IRLS algorithm using gradient linearization

The direct implementation of [6] would involve the non-linear mapping between the images \mathbf{x}_i and their non-linear maps $\phi(\mathbf{x}_i)$ and their inverse as described in (33). However, this approach is computationally infeasible in our setting since the dimension of the feature matrix $\Phi(\mathbf{X})$ is too large. Hence, we propose to use an algorithm that relies on the Gram matrix of $\Phi(\mathbf{X})$, denoted by $\mathcal{K}(\mathbf{X}) = \Phi(\mathbf{X})^H \Phi(\mathbf{X})$ and referred to as the kernel matrix; this approach is known as the kernel trick in machine learning. For the specific choice of exponential maps as in [5], we obtain the Gaussian kernel:

$$[\mathcal{K}(\mathbf{X})]_{i,j} = \exp\left(-\frac{\|\mathbf{x}_i - \mathbf{x}_j\|^2}{2\sigma^2}\right). \quad [7]$$

We propose to use the IRLS scheme with gradient linearization (31, 32) to solve [6]. This scheme alternates between

$$\mathbf{X}^i = \arg \min_{\mathbf{X}} \|\mathcal{A}(\mathbf{X}) - \mathbf{B}\|_F^2 + \text{trace}(\mathbf{X} \underbrace{(\lambda_1 \mathbf{L}^{(i)} + \lambda_2 \mathbf{L}_n)}_{\mathbf{L}_{\text{eq}}} \mathbf{X}^H) \quad [8]$$

and update of the matrix $\mathbf{L}^{(i)}$:

$$\mathbf{L}^{(i)} = \mathbf{D} \left(\mathbf{W}^{(i)} \right) - \mathbf{W}^{(i)}. \quad [9]$$

Here, the weight matrix at the i^{th} iteration is specified by

$$\mathbf{W}^{(i)} = -\frac{1}{\sigma^2} \mathcal{K} \left(\mathbf{X}^{(i-1)} \right) \odot \left[\mathcal{K} \left(\mathbf{X}^{(i-1)} \right) + \gamma \mathbf{I} \right]^{-\frac{1}{2}}, \quad [10]$$

where $\mathcal{K}(\mathbf{X})$ is the kernel matrix in [7].

Two-step approach to improve computational efficiency

The above algorithm alternates between the update of the high-resolution images, specified by [8] and update of the Laplacian matrix, specified by [9]. The computation cost associated with this scheme is high, especially when used with large number of high-resolution images. To improve computational efficiency, we propose to first recover the low-resolution images from the central k-space samples of the high-resolution images as shown in Fig. 1. Note that the low-resolution images are still undersampled. We use the alternat-

ing scheme to recover the low-resolution images with reduced alias artifacts, while providing the Laplacian matrix that is not corrupted by aliasing artifacts in the images. The smaller size of the images translates to a faster algorithm. Once the above algorithm converges, the estimated Laplacian matrix is then used to recover the high-resolution image frames from their undersampled measurements by solving [8] as shown Fig. 1. Note that we do not alternate between Laplacian update and image update in the high-resolution setting, thus resulting in a fast algorithm.

Simulation dataset

A retrospective ECG-gated, breath-held cardiac MRI is used to create a simulated ungated, free breathing data, as described in (36). The breath-held dataset is warped in space and time to mimic respiratory motion and temporally varying heart rate. The deformed datasets are combined to form an image sequence with multiple cardiac cycles. This simulated dataset enables the quantitative comparison of methods, especially in the free-breathing setting where ground truth is not available.

Acquisition scheme

Cardiac data were collected in the free breathing mode from four volunteers using golden angle spiral trajectory. The institutional review board at the local institution approved all the in-vivo acquisitions and written consent was obtained from all subjects. The sequence parameters were: TR/TE= 7.8 ms, FOV=320 mm, Base resolution=256, Bandwidth= 390 Hz/pixel, flip angle= 15 degrees, slice thickness= 8 mm. Dual-density spirals were generated using a Fermi function with a k-space density of 0.2x Nyquist for the first 20% of the trajectory and an ending density of 0.02x Nyquist (37). The spirals were continuously acquired. Post-acquisition, we binned five spirals per frame to obtain the temporal resolution of 40 ms. The parameters of our reconstruction algorithm were manually optimized on one dataset and kept fixed for rest of the datasets.

Experiments

We demonstrate the two-step recovery scheme in Fig 2. Specifically, we show the recovered low-resolution images corresponding to a different number of iterations of the kernel low-rank regularization, which alternates between [9] and [8]. The Laplacian matrix obtained from each of the reconstructions in the top row are used to recover the high-resolution images in the second row.

We validate the algorithm on simulated data in Fig 3. We compare the low-rank (Schatten p norm minimization $p = 0.5 - 1$), first iteration of the STORM method, and the proposed STORM method that relies on kernel low-rank regularization in Fig 3. The first iteration of the STORM scheme estimates the Laplacian matrix from the CG-SENSE reconstructions of the images, followed by the STORM reconstructions; the Laplacian matrix is not optimized in an iterative fashion. By contrast, the proposed scheme starts with the CG-SENSE initialization and iterates between the estimation of the Laplacian matrix and the update of the images. The quantitative results are shown in the Table 1. The results show that the proposed scheme provides significantly improved results as compared to the low-rank and the first iteration of STORM, which estimates the Laplacian matrix from the low-resolution SENSE images.

The comparison of our method against the low-rank and the first iteration of STORM is shown in Fig 4, in the context of experimental data. Since no ground truth is available, the regularization parameters were hand tuned manually to yield the best possible results for each algorithm. We optimized the parameters for one dataset, which were then used for all reconstructions.

We compare the proposed scheme against the XD-GRASP algorithm in Fig. 5 and 6. XD-GRASP is a self-gated strategy, which estimates the cardiac and respiratory phases from center sample of k-space regions (24). It estimates the cardiac and respiratory signals by applying band-pass filtering as both motions correspond to the different frequencies. The estimated cardiac and respiratory phases are overlaid on the time profiles in the top left figure. Using these signals, the k-space data is sorted into cardiac and respiratory bins. Compressed sensing based reconstruction algorithm is then used to recover the images, by exploiting the sparsity along two dynamic dimensions. We used the author-provided MATLAB code for XD-GRASP implementation (24). Since XD-GRASP and the proposed scheme are using different reconstruction methodologies, we illustrate the results in two ways. In Fig. 5, we display the reconstructed images in the different cardiac and respiratory phases in the bottom rows, which are identified by XD-GRASP. We create a cine movie by picking each image in the time series from the XD-GRASP reconstructions depending on the specified cardiac and respiratory phase; the time profile in the top row corresponds to a cut along the myocardium identified by the blue line in one of the images. We also display the rows of the weight matrix \mathbf{W} corresponding to two frames, identified by the yellow and red arrows in the top right columns. As discussed earlier, the weights indicate the similarity of the specific frame with other frames in the dataset. We also show the zoomed versions of a cardiac cycle in the XD-GRASP and the proposed scheme in Fig. 6.

RESULTS

The results in Fig. 2 show the benefit of the iterative strategy. Specifically, the first column shows the STORM reconstructions using the Laplacian estimated from SENSE reconstruction, which is the first iteration of the proposed scheme. We observe that this Laplacian estimate results in the poor low-resolution reconstruction with residual aliasing artifacts. By contrast, we note that the iterative strategy reduces the alias artifacts and improves the spatial resolution. In particular, the alias artifacts are reduced with iterations. The Laplacian estimated from the fifth iteration yields improved reconstructions with the reduced artifacts in the liver regions and the minimal myocardial blurring. These observations are also seen from Table 1, where the iterative algorithm improves the signal to error ratio by over 11 dB compared to the first iteration STORM. We note that the computational complexity associated by the iterative kernel low-rank algorithm is low when it is used to solve low-resolution images. By contrast, the high-resolution recovery scheme relies on the Laplacian matrix, estimated from the low-resolution data.

Fig. 3 shows the performance comparison between the proposed method, low-rank scheme and "1st iteration STORM" method on the numerical phantom dataset, while the quantitative results are shown in Table 1. We observe that the proposed scheme significantly reduces the spatial and temporal blurring compared to the low-rank scheme, which demonstrates the ability of the kernel low-rank algorithm in capturing non-linear redundancies. The comparison between the third and fourth rows shows the improvement in the performance with iterations. The error images also show the significantly reduced errors associated with the proposed scheme. The quantitative comparisons of the schemes using different metrics are shown in Table 1.

We compare the performance of the algorithms on two experimental datasets in Fig. 4. We have picked three frames (end of diastole, mid frame, end of systole) from the image series to show the spatial quality of the proposed method as compared to the low-rank method and "1st iteration STORM", where the Laplacian matrix is estimated from SENSE reconstructions. The fourth column of Fig. 4 shows the temporal profiles. We observe that the proposed scheme provides better spatial quality compared to the low-rank method and "1st iteration STORM" scheme, while also reducing the temporal blurring.

Fig 5 & Fig.6 show the performance comparison between the proposed method and XD-GRASP (24). The top row in Fig. 5.a shows the temporal profile of XD-GRASP, while the corresponding temporal profiles of the proposed scheme is shown in Fig. 5.b. We note that the cardiac and respiratory phases identified

by XD-GRASP are roughly in agreement with the motion patterns in the temporal profiles of the proposed scheme in Fig. 5.b. By contrast, the motion patterns in the temporal profiles in XD-GRASP appear attenuated. We also observe sharp transitions in contrast between frames from different cardiac/respiratory phases. The top rows of Fig. 5.(b) show the weights corresponding to two frames in end inspiration and end expiration, respectively. Note that the weight patterns agree reasonably well visually with the identified cardiac respiratory phases. The weights indicate soft-binning of the phases offered by the proposed scheme. The bottom rows of Fig. 5 show the reconstructed images arranged in the cardiac and respiratory phases. Fig. 5.a shows the recovered images using XD-GRASP, while Fig. 5.b corresponds to the proposed method. We note that some of the phase images are blurred in the XD-GRASP reconstructions. These phases correspond to the poorly sampled cardiac and respiratory phases. The soft-binning offered by the weighting strategy allows for more data-sharing between the phases, resulting in reduced myocardial blurring and improved fidelity of the temporal profiles.

The zoomed versions of the reconstructions of a cardiac cycle from two subjects, obtained using XD-GRASP and the proposed scheme, are shown in reconstructions Fig.6. We note that temporal profiles are roughly matching. However, the proposed scheme exhibits reduced temporal blurring. Similarly, the comparison of the spatial frames also demonstrates the reduced blurring offered by the soft-binning strategy.

DISCUSSION

We introduced an iterative spiral-SToRM framework for the recovery of free-breathing and ungated cardiac images from 2-D spiral acquisition. We assume the images lie on a smooth manifold, and rely on a manifold smoothness prior to recover the dataset. The main difference of this scheme with our prior work (29) is use of an iterative kernel low-rank algorithm for the estimation of the Laplacian from undersampled data. The proposed approach eliminates the need for explicit k-space navigators, and instead relies on variable-density spiral acquisitions, where the central k-space regions are acquired with higher density. The manifold Laplacian is estimated from central k-space regions. We rely on a two-step strategy, where the low-resolution reconstructions as well as the Laplacian are estimated from a central region with higher k-space density. The Laplacian estimation from undersampled data is posed as an optimization scheme. Once the Laplacian is estimated, we solve for the high-resolution image from the entire k-space data using manifold smoothness regularization. We also approximate the Laplacian using a few basis functions, which reduces the compu-

tational complexity and memory demand of the algorithm by an order of magnitude. To summarize, the iterative SToRM approach recovers 2D cine images with reduced spatial and temporal blurring in a short free-breathing self-gated acquisition, compared to low-rank and explicit binning strategies. Due to its computational efficiency and lack of need for manual intervention, this method may be a good candidate for clinical scans where patients (e.g. heart failure, pediatric or obese subjects) are unable to hold their breath for sufficiently long periods of time, or are unable to follow breath-holding instructions. In the future, the proposed scheme can be extended to multi-slice acquisitions, either using 3-D or simultaneous multi-slice strategies.

The gradient echo (GRE) strategy may have a few advantages for simplifying 3T cine imaging, even though SSFP sequences are typically used for cine imaging. The longer TR associated with the spiral trajectory provides sufficient time for inflow-enhancement of the LV blood pool; the resulting contrast is similar to the Cartesian SSFP imaging as compared to the shorter TR Cartesian GRE imaging. In addition, the proposed spoiled GRE-based approach is robust to banding artifacts, which SSFP methods are vulnerable to and therefore, no frequency scout is needed for the proposed scheme. In addition, GRE schemes are less sensitive to eddy current artifacts caused by the large angular increment of the golden angle ordering (38). With 16 seconds per slice, the whole heart can be imaged in 3 minutes.

The spiral-based acquisitions may become more sensitive to off-resonance artifacts as the readout duration increases. However, we did not experience significant blurring in our scans with readout durations of 3-5 ms. Off-resonance correction strategies may be used to further reduce blurring. Another challenge with GRE based acquisition compared to the traditional SSFP approach is the lower SNR and CNR. This problem is partially mitigated by the use of longer TR and higher flip angles.

The proposed method produces a series of ungated images in different respiratory phases; images from matching respiratory phases from different slices may be combined post-reconstruction for the estimation of functional parameters; this approach thus may reduce errors due to mismatches in breath-holding locations, which is often a problem with breath-held cine. The real-time like recovery also enables the user to visualize the data with both respiratory and cardiac motion. This approach may be useful in studies on patients with heart failure or pulmonary complications such as COPD. The data can also be automatically segmented into respiratory and cardiac phases post reconstruction for easy visualization of the data, using the eigenvectors of the estimated Laplacian matrix.

TABLE 1			
Method	SER	SSIM	HFEN
Low Rank	18.68	0.835	0.372
1st Iter SToRM	18.96	0.807	0.380
Proposed	30.44	0.977	0.041

Table 1: Quantitative comparison of the methods on simulated data in Fig. 3 using SER, HFEN, and SSIM metrics. All of these metrics are computed in a square region of interest around the cardiac region. These comparisons show that the proposed scheme significantly outperforms both of the other methods.

CONCLUSION

In this paper, we have proposed an iterative SToRM for the navigator-less free-breathing and ungated cardiac MR data. Simulations and validations are performed on human subjects using spiral-based acquisition. These results show the ability of the scheme in providing image reconstructions with reduced spatial and temporal blurring from a short free-breathing self-gated acquisition, compared to state-of-the-art methods.

Legends

Fig 1: Outline of the Spiral-SToRM method. Free breathing and ungated data is acquired using a golden angle spiral acquisition scheme. To realize a computationally efficient algorithm, we rely on a two-step strategy; a low-resolution dataset is first recovered, followed by the reconstruction of the high-resolution images. In the first step, we estimate the Laplacian matrix using an iterative kernel low-rank based method from the central k-space regions, illustrated with a square. Note that this region is still not fully sampled; we propose to recover all the k-space samples, and equivalently the low-resolution images, using kernel low-rank regularization. This algorithm solves [6] by an iterative algorithm that alternates between [8] and the update of the Laplacian specified by [9]. As described in the text, this iterative strategy yields the Laplacian matrix as a by-product. The Laplacian matrix entries describe the connectivity of the points of the manifold, with larger weights between similar frames in the dataset. Once the Laplacian is available, the high-resolution dataset is estimated from all of the k-space samples by solving [8].

Fig 2: Illustration of the two-step algorithm and variation of image quality with iterations. The proposed algorithm relies on kernel low-rank minimization to recover the low-resolution images, and in the process estimates the Laplacian matrix. (a) low-resolution image, corresponding to the first iteration of the kernel low-rank algorithm. The image is recovered using [8], where the Laplacian matrix is estimated from a SENSE recovered low-resolution dataset. The use of this Laplacian matrix yields the high-resolution image, shown in (d). Note that both (a) and (d) suffers from blurring artifacts, corresponding to unresolved motion. (b)&(e). High and low-resolution images corresponding to the second iteration. (c)&(f). High and low-resolution images corresponding to the fifth iteration. Note that the spiral artifacts are significantly attenuated, while the image also suffers from less blurring in (b)&(d). Red arrows are employed to pinpoint the reduction in blurring artifacts as we increase the number of iterations.

Fig 3: Validation of the algorithm using simulated short axis cardiac cine dataset. We compare the low-rank algorithm (b1-b3), 1st Iteration of SToRM method (c1-c3), and the proposed method (d1-d3). Each scheme is compared against the original dataset (a1-a3). This dynamic dataset is retrospectively undersampled using golden angle spiral sampling pattern. Three cardiac phases are picked from each reconstruction method which correspond to end of systolic, mid phase, and end of diastolic as shown by red, yellow, green lines in the time profile (a4) . The time profiles in the last column are shown for the entire time series, along the line passing through the left ventricle and right ventricle shown in (a3). We observe that the proposed method provides reconstructions with lower spatial and

temporal blurring, compared to other algorithms. The residual images depict that the proposed method provides better preservation of fine features, including papillary muscles. On the other hand, the residual images which correspond to low-rank method and 1st Iteration SToRM, show the blurring artifacts. Table 1 shows a quantitative comparison of the methods using SER, HFEN, and SSIM metrics computed around the cardiac region

Fig 4: Comparison against free-breathing methods without binning: We compare the proposed scheme against low-rank (Schatten p ; $p = 0.5$ norm minimization) approach and the first iteration of our algorithm, where the Laplacian matrix is estimated from SENSE reconstructions of the undersampled spiral data. Temporal profiles are also shown for the whole acquisition. We note that the proposed scheme reduces blurring of the spatial images as well as the temporal profiles. Red dotted rectangles are used to show comparison of a cardiac cycle. In the low-rank method, transition from the end of diastole phase to the end of systole is not smooth as compared to the other two methods. The 1st Iter SToRM method has more blurring as compared to the proposed method.

Fig 5: Comparison to XD-GRASP: Since both methods use different reconstruction strategies, we rearrange the images obtained using SToRM into respiratory and cardiac phases in (b) for direct comparison to the cardiac and respiratory phases reconstructed using XD-GRASP in (a). We also re-arrange the XD-GRASP recovered frames to form a temporal profile, in the top-row. Specifically, we constructed a time series by picking the XD-GRASP frames corresponding to the identified cardiac and respiratory phases. We observe that some of the cardiac/respiratory phases are not well sampled in XD-GRASP due to variable breathing cycles, resulting in blurring and aliasing artifacts. See phases outlined by green boxes. By contrast, our soft-binning strategy exploits the similarity between the phases along the time series to reduce these artifacts. The weight patterns for two frames indicated by the yellow and red arrows are shown in the top row. We note that the weights are high whenever the frames are similar to the chosen frame; the algorithm combines the information in these similar frames to obtain high-resolution reconstructions.

Fig 6: Comparison of the proposed scheme against XD-GRASP. We show the frames from our dataset that closely match the ones recovered using XD-GRASP. Note that we do not expect a perfect match in anatomy since XD-GRASP performs an averaging of data within respiratory bins. Three spatial frames are shown, picked from the locations indicated in the temporal profiles with red, green blue lines. The proposed method has less blurring as compared to the XDGRASP method, as the XDGRASP method is averaging the data within a respiratory state. White arrows are used to show the end systole phase, which is well captured by both methods.

References

- 1 Spencer B. Gay, Chris L. Siström, Chad A. Holder, and Paul M. Suratt. Breath-Holding Capability of Adults: Implications for Spiral Computed Tomography, Fast-Acquisition Magnetic Resonance Imaging, and Angiography. *Investigative Radiology*, 29, 1994.
- 2 Zhi-Pei Liang, Hong Jiang, Christopher P Hess, and Paul C Lauterbur. Dynamic imaging by model estimation. *International journal of imaging systems and technology*, 8(6):551–557, 1997.
- 3 Behzad Sharif, J Andrew Derbyshire, Anthony Z Faranesh, and Yoram Bresler. Patient-adaptive reconstruction and acquisition in dynamic imaging with sensitivity encoding (paradise). *Magnetic Resonance in Medicine*, 64(2):501–513, 2010.
- 4 Jeffrey Tsao, Peter Boesiger, and Klaas P Pruessmann. k-t blast and k-t sense: Dynamic mri with high frame rate exploiting spatiotemporal correlations. *Magnetic resonance in medicine*, 50(5):1031–1042, 2003.
- 5 Hong Jung, Kyunghyun Sung, Krishna S Nayak, Eung Yeop Kim, and Jong Chul Ye. k-t focuss: a general compressed sensing framework for high resolution dynamic mri. *Magnetic resonance in medicine*, 61(1):103–116, 2009.
- 6 Michael Lustig, Juan M Santos, David L Donoho, and John M Pauly. kt sparse: High frame rate dynamic mri exploiting spatio-temporal sparsity. In *Proceedings of the 13th Annual Meeting of ISMRM, Seattle*, volume 2420, 2006.
- 7 Bo Zhao, Justin P Haldar, Anthony G Christodoulou, and Zhi-Pei Liang. Image reconstruction from highly undersampled (k, t)-space data with joint partial separability and sparsity constraints. *IEEE transactions on medical imaging*, 31(9):1809–1820, 2012.
- 8 Bo Zhao, Justin P. Haldar, and Zhi-Pei Liang. PSF Model-Based Reconstruction with Sparsity Constraint: Algorithm and Application to Real-Time Cardiac MRI. *Annual International Conference of the IEEE Engineering in Medicine and Biology Society.*, 2010:3390–3393, 2010.

- 9 Sajjan Goud Lingala, Yue Hu, Edward DiBella, and Mathews Jacob. Accelerated dynamic mri exploiting sparsity and low-rank structure: kt slr. *IEEE transactions on medical imaging*, 30(5):1042–1054, 2011.
- 10 Sajjan Goud Lingala, Edward DiBella, Ganesh Adluru, Christopher McGann, and Mathews Jacob. Accelerating free breathing myocardial perfusion mri using multi coil radial k- t slr. *Physics in Medicine & Biology*, 58(20):7309, 2013.
- 11 Sajjan Goud Lingala and Mathews Jacob. A blind compressive sensing framework for accelerated dynamic mri. In *IEEE International Symposium on Biomedical Imaging*, 2012.
- 12 Sajjan Goud Lingala and Mathews Jacob. Blind compressive sensing dynamic mri. *IEEE transactions on medical imaging*, 32(6):1132–1145, 2013.
- 13 M Salman Asif, Lei Hamilton, Marijn Brummer, and Justin Romberg. Motion-adaptive spatio-temporal regularization for accelerated dynamic mri. *Magnetic Resonance in Medicine*, 70(3):800–812, 2013.
- 14 Yasir Q. Mohsin, Sajjan Goud Lingala, Edward DiBella, and Mathews Jacob. Accelerated dynamic mri using patch regularization for implicit motion compensation. *Magnetic Resonance in Medicine*, 77(3):1238–1248, 2017.
- 15 Yasir Q Mohsin, Sajjan Goud Lingala, Edward DiBella, and Mathews Jacob. Accelerated dynamic mri using patch regularization for implicit motion compensation. *Magnetic resonance in medicine*, 77(3):1238–1248, 2017.
- 16 Ukash Nakarmi, Yanhua Wang, Jingyuan Lyu, Dong Liang, and Leslie Ying. A kernel-based low-rank (klr) model for low-dimensional manifold recovery in highly accelerated dynamic mri. *IEEE transactions on medical imaging*, 36(11):2297–2307, 2017.
- 17 Sergio Uribe, Vivek Muthurangu, Redha Boubertakh, Tobias Schaeffter, Reza Razavi, Derek LG Hill, and Michael S Hansen. Whole-heart cine mri using real-time respiratory self-gating. *Magnetic Resonance in Medicine*, 57(3):606–613, 2007.
- 18 Sergio Uribe, Philipp Beerbaum, Thomas Sangild Sørensen, Allan Rasmusson, Reza Razavi, and Tobias Schaeffter. Four-dimensional (4d) flow of the whole heart and great vessels using real-time respiratory self-gating. *Magnetic Resonance in Medicine: An Official Journal of the International Society for Magnetic Resonance in Medicine*, 62(4):984–992, 2009.

- 19 Xue Feng, Michael Salerno, Christopher M Kramer, and Craig H Meyer. Non-cartesian balanced steady-state free precession pulse sequences for real-time cardiac mri. *Magnetic resonance in medicine*, 75(4):1546–1555, 2016.
- 20 David Firmin and Jenny Keegan. Navigator echoes in cardiac magnetic resonance. *Journal of Cardiovascular Magnetic Resonance*, 3(3):183–193, 2001.
- 21 Bernd Jung, Maxim Zaitsev, Jürgen Hennig, and Michael Markl. Navigator gated high temporal resolution tissue phase mapping of myocardial motion. *Magnetic Resonance in Medicine: An Official Journal of the International Society for Magnetic Resonance in Medicine*, 55(4):937–942, 2006.
- 22 Dana C Peters, Reza Nezafat, Holger Eggers, Christian Stehning, and Warren J Manning. 2d free-breathing dual navigator-gated cardiac function validated against the 2d breath-hold acquisition. *Journal of Magnetic Resonance Imaging: An Official Journal of the International Society for Magnetic Resonance in Medicine*, 28(3):773–777, 2008.
- 23 Li Feng, Robert Grimm, Kai Tobias Block, Hersh Chandarana, Sunghoon Kim, Jian Xu, Leon Axel, Daniel K Sodickson, and Ricardo Otazo. Golden-angle radial sparse parallel mri: Combination of compressed sensing, parallel imaging, and golden-angle radial sampling for fast and flexible dynamic volumetric mri. *Magnetic resonance in medicine*, 72(3):707–717, 2014.
- 24 Li Feng, Leon Axel, Hersh Chandarana, Kai Tobias Block, Daniel K Sodickson, and Ricardo Otazo. Xd-grasp: Golden-angle radial mri with reconstruction of extra motion-state dimensions using compressed sensing. *Magnetic resonance in medicine*, 75(2):775–788, 2016.
- 25 Jingfei He, Qiegen Liu, Anthony G Christodoulou, Chao Ma, Fan Lam, and Zhi-Pei Liang. Accelerated high-dimensional mr imaging with sparse sampling using low-rank tensors. *IEEE transactions on medical imaging*, 35(9):2119–2129, 2016.
- 26 Ruixi Zhou, Wei Huang, Yang Yang, Xiao Chen, Daniel S Weller, Christopher M Kramer, Sebastian Kozerke, and Michael Salerno. Simple motion correction strategy reduces respiratory-induced motion artifacts for kt accelerated and compressed-sensing cardiovascular magnetic resonance perfusion imaging. *Journal of Cardiovascular Magnetic Resonance*, 20(1):6, 2018.

- 27 Zhou Ruixi, Yang Yang, Mathew Roshin, and Salerno Michael. Cardiac and respiratory self-gated motion-corrected free-breathing spiral cine imaging. In *Joint annual meetings ismrm-esmrm, 16-21 June*. ISMRM, 2018.
- 28 Teodora Chitiboi, Li Feng, Rebecca Ramb, Ricardo Otazo, and Leon Axel. reconstruction of arrhythmic cardiac cycle in patients with atrial fibrillation. In *Joint Annual Meeting ISMRM-ESMRMB*. ISMRM, 2018.
- 29 S. Poddar and M. Jacob. Dynamic mri using smoothness regularization on manifolds (storm). *IEEE Tran. Medical Imaging*, 35(4):1106–1115, April 2016.
- 30 S. Poddar, Y. Mohsin, A. Deidra, B. Thattayilath, R. Ashwath, and M. Jacob. Manifold recovery using kernel low-rank regularization: application to dynamic imaging. *IEEE Transactions on Computational Imaging*, in press, 2018.
- 31 Sunrita Poddar and Mathews Jacob. Recovery of noisy points on band-limited surfaces: Kernel methods re-explained. *arXiv preprint arXiv:1801.00890*, 2018.
- 32 Sunrita Poddar and Mathews Jacob. Recovery of point clouds on surfaces: Application to image reconstruction. In *Biomedical Imaging (ISBI 2018), 2018 IEEE 15th International Symposium on*, pages 1272–1275. IEEE, 2018.
- 33 U. Nakarmi, Y. Wang, J. Lyu, D. Liang, and L. Ying. A kernel-based low-rank (klr) model for low-dimensional manifold recovery in highly accelerated dynamic mri. *IEEE Transactions on Medical Imaging*, PP(99):1–1, 2017.
- 34 Bo Zhao, Justin P Haldar, and Zhi-Pei Liang. Psf model-based reconstruction with sparsity constraint: Algorithm and application to real-time cardiac mri. In *Engineering in Medicine and Biology Society (EMBC), 2010 Annual International Conference of the IEEE*, pages 3390–3393. IEEE, 2010.
- 35 Guy Gilboa and Stanley Osher. Nonlocal operators with applications to image processing. *Multiscale Modeling & Simulation*, 7(3):1005–1028, 2008.
- 36 Bo Zhao, Justin P Haldar, Anthony G Christodoulou, and Zhi-Pei Liang. Image reconstruction from highly undersampled (k, t)-space data with joint partial separability and sparsity constraints. *IEEE transactions on medical imaging*, 31(9):1809–1820, 2012.

- 37 Yang Yang, Christopher M Kramer, Peter W Shaw, Craig H Meyer, and Michael Salerno. First-pass myocardial perfusion imaging with whole-heart coverage using 11-spiral accelerated variable density spiral trajectories. *Magnetic resonance in medicine*, 76(5):1375–1387, 2016.
- 38 Stefan Wundrak, Jan Paul, Johannes Ulrici, Erich Hell, Margrit-Ann Geibel, Peter Bernhardt, Wolfgang Rottbauer, and Volker Rasche. Golden ratio sparse mri using tiny golden angles. *Magnetic resonance in medicine*, 75(6):2372–2378, 2016.

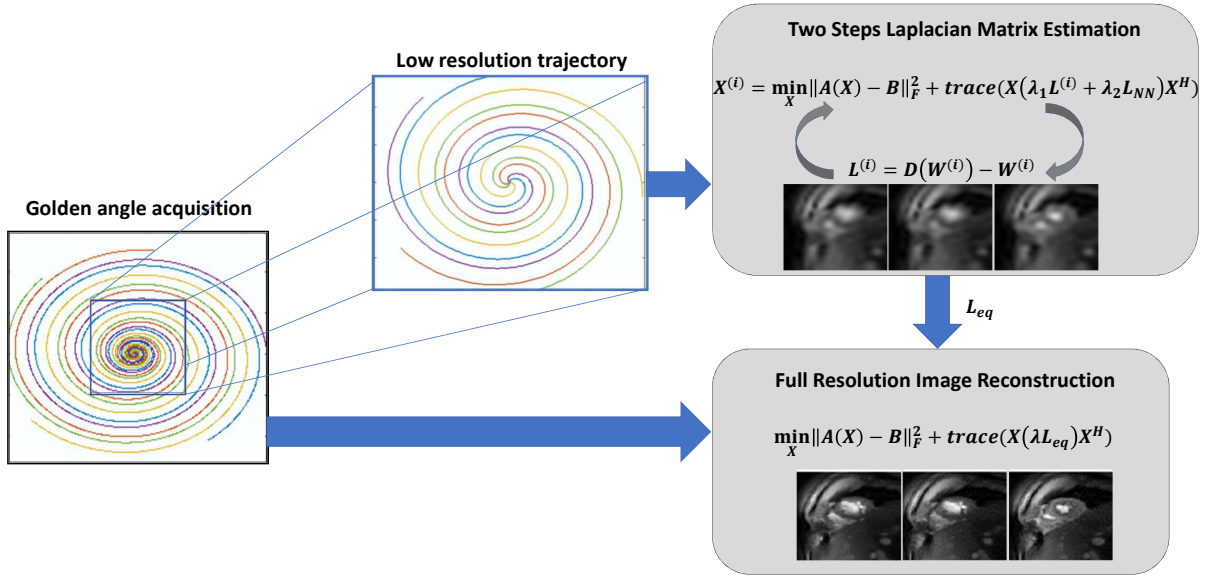


Figure 1: Outline of the Spiral-SToRM method. Free breathing and ungated data is acquired using a golden angle spiral acquisition scheme. To realize a computationally efficient algorithm, we rely on a two-step strategy; a low-resolution dataset is first recovered, followed by the reconstruction of the high-resolution images. In the first step, we estimate the Laplacian matrix using an iterative kernel low-rank based method from the central k-space regions, illustrated with a square. Note that this region is still not fully sampled; we propose to recover all the k-space samples, and equivalently the low-resolution images, using kernel low-rank regularization. This algorithm solves [6] by an iterative algorithm that alternates between [8] and the update of the Laplacian specified by [9]. As described in the text, this iterative strategy yields the Laplacian matrix as a by-product. The Laplacian matrix entries describe the connectivity of the points of the manifold, with larger weights between similar frames in the dataset. Once the Laplacian is available, the high-resolution dataset is estimated from all of the k-space samples by solving [8].

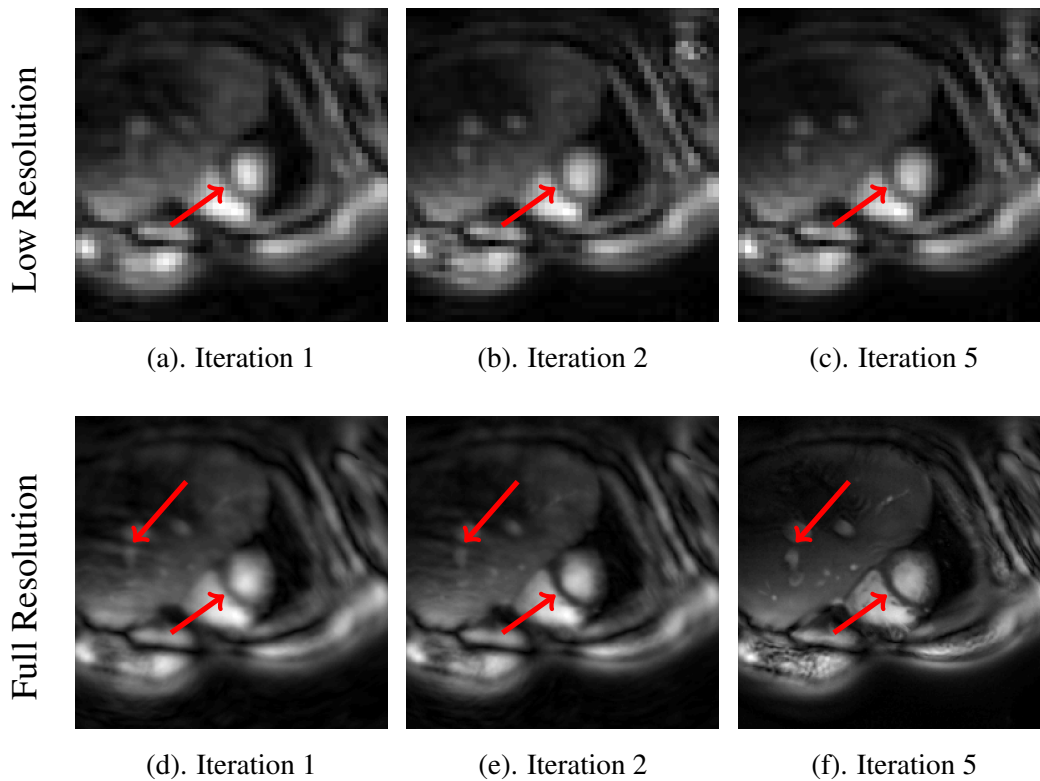


Figure 2: Illustration of the two-step algorithm and variation of image quality with iterations. The proposed algorithm relies on kernel low-rank minimization to recover the low-resolution images, and in the process estimates the Laplacian matrix. (a) low-resolution image, corresponding to the first iteration of the kernel low-rank algorithm. The image is recovered using [8], where the Laplacian matrix is estimated from a SENSE recovered low-resolution dataset. The use of this Laplacian matrix yields the high-resolution image, shown in (d). Note that both (a) and (d) suffers from blurring artifacts, corresponding to unresolved motion. (b)&(e). High and low-resolution images corresponding to the second iteration. (c)&(f). High and low-resolution images corresponding to the fifth iteration. Note that the spiral artifacts are significantly attenuated, while the image also suffers from less blurring in (b)&(d). Red arrows are employed to pinpoint the reduction in blurring artifacts as we increase the number of iterations.

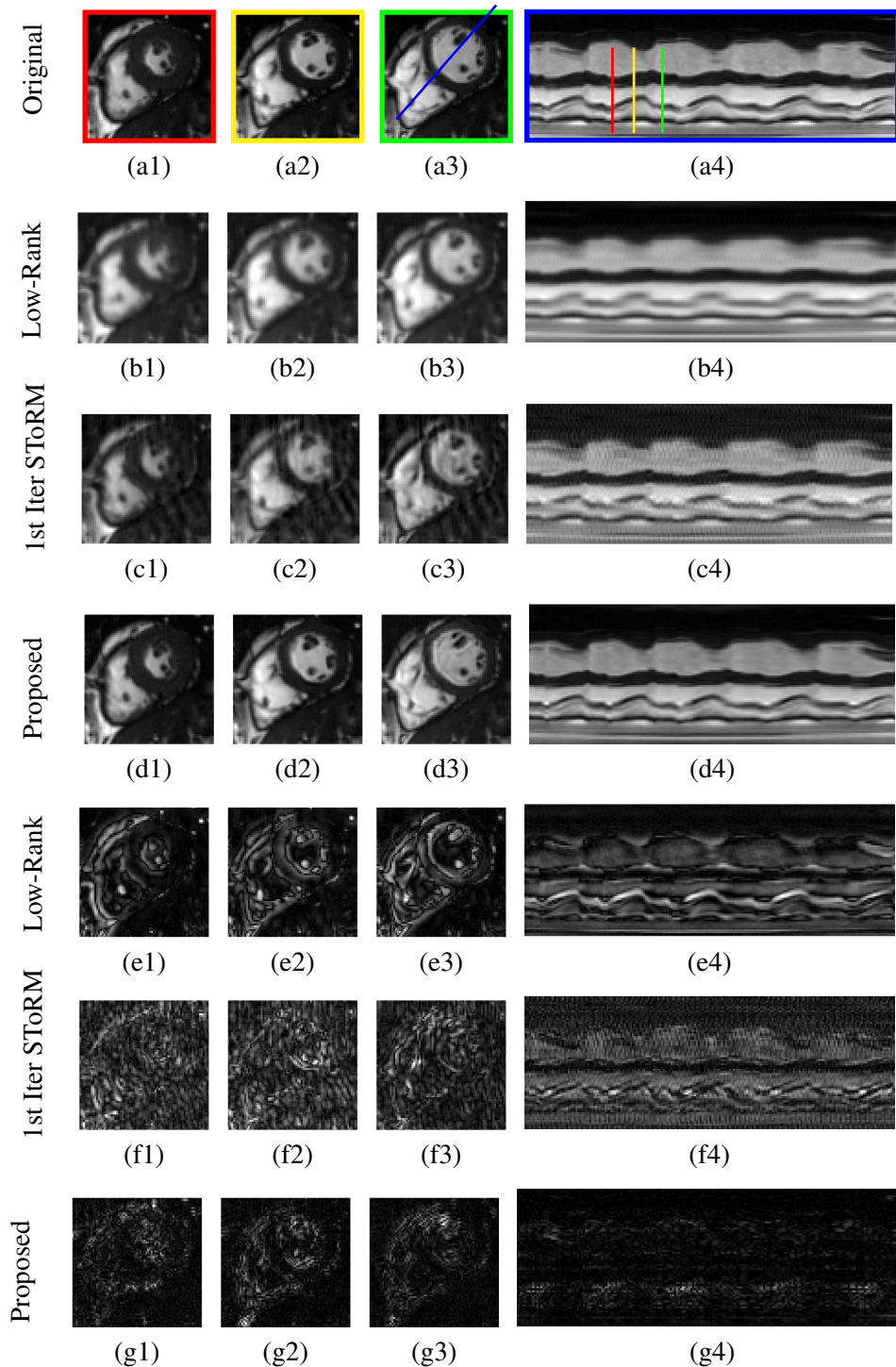


Figure 3: Validation of the algorithm using simulated short axis cardiac cine dataset. We compare the low-rank algorithm (b1-b3), 1st Iteration of SToRM method (c1-c3), and the proposed method (d1-d3). Each scheme is compared against the original dataset (a1-a3). This dynamic dataset is retrospectively undersampled using golden angle spiral sampling pattern. Three cardiac phases are picked from each reconstruction method which correspond to end of systolic, mid phase, and end of diastolic as shown by red, yellow, green lines in the time profile (a4). The time profiles in the last column are shown for the entire time series, along the line passing through the left ventricle and right ventricle shown in (a3). We observe that the proposed method provides reconstructions with lower spatial and temporal blurring, compared to other algorithms. The residual images depict that the proposed method provides better preservation of fine features, including papillary muscles. On the other hand, the residual images which correspond to low-rank method and 1st Iteration SToRM, show the blurring artifacts. Table 1 shows a quantitative comparison of the methods using SER, HFEN, and SSIM metrics computed around the cardiac region

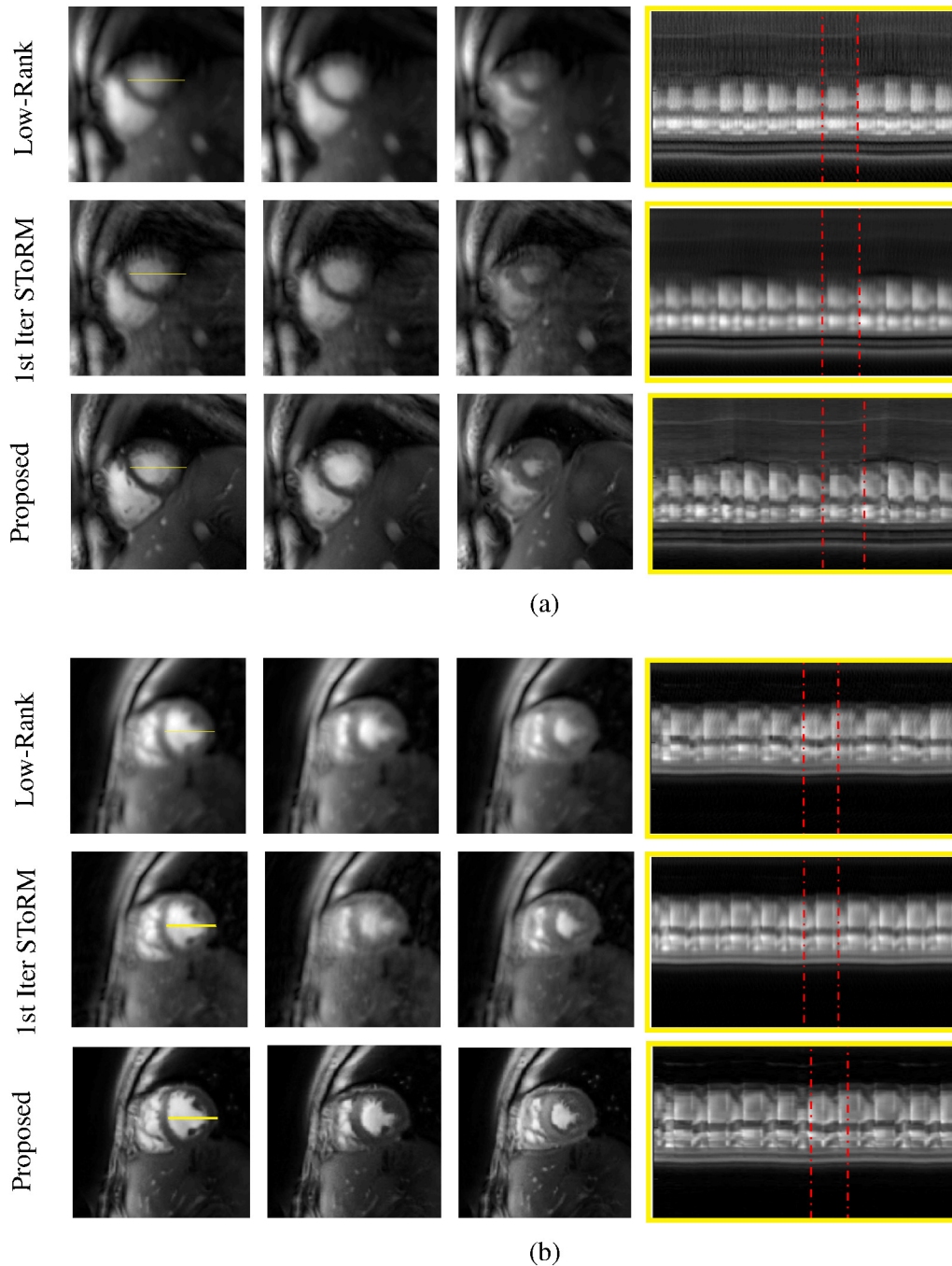


Figure 4: Comparison against free-breathing methods without binning: We compare the proposed scheme against low-rank (Schatten p ; $p = 0.5$ norm minimization) approach and the first iteration of our algorithm, where the Laplacian matrix is estimated from SENSE reconstructions of the undersampled spiral data. Temporal profiles are also shown for the whole acquisition. We note that the proposed scheme reduces blurring of the spatial images as well as the temporal profiles. Red dotted rectangles are used to show comparison of a cardiac cycle. In the low-rank method, transition from the end of diastole phase to the end of systole is not smooth as compared to the other two methods. The 1st Iter SToRM method has more blurring as compared to the proposed method.

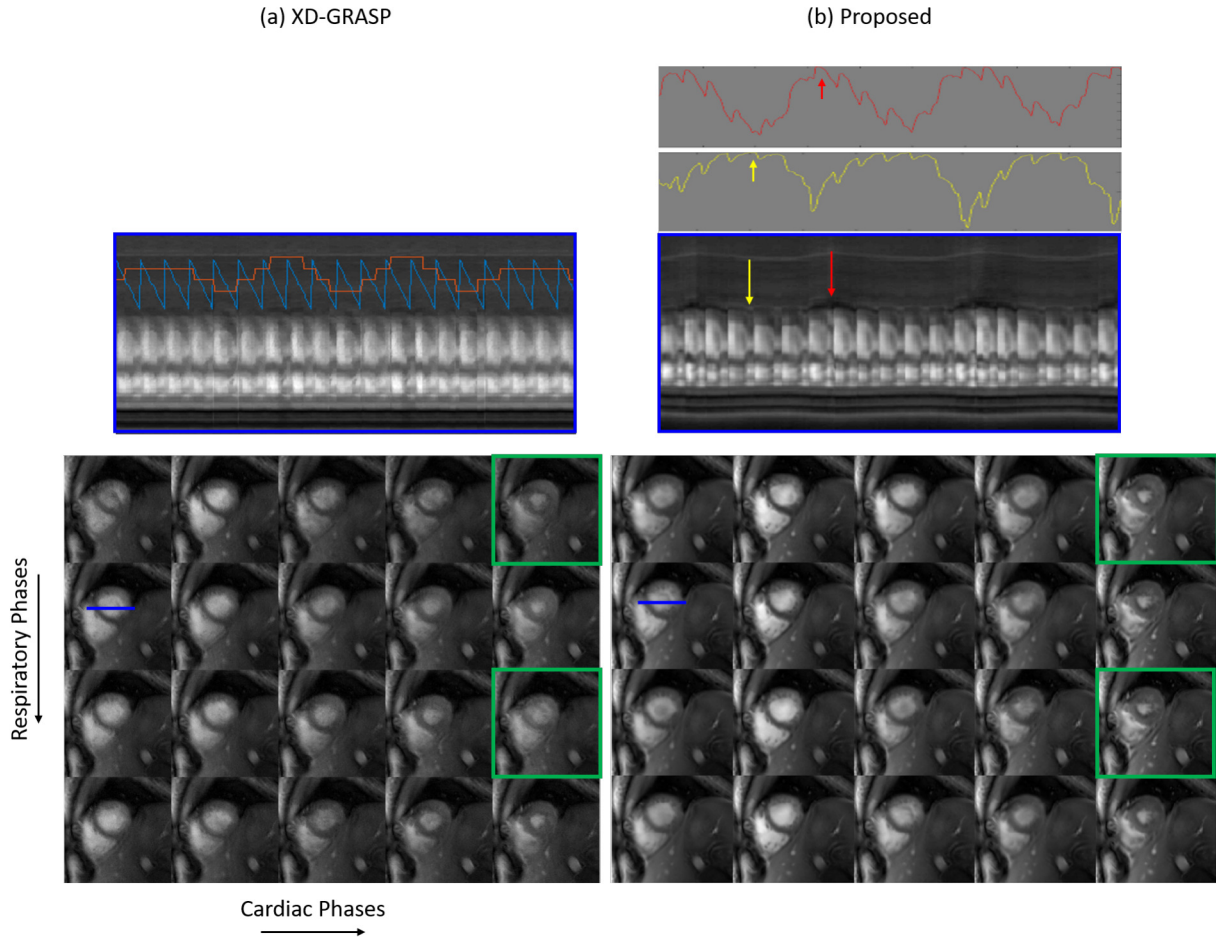


Figure 5: Comparison to XD-GRASP: Since both methods use different reconstruction strategies, we rearrange the images obtained using STORM into respiratory and cardiac phases in (b) for direct comparison to the cardiac and respiratory phases reconstructed using XD-GRASP in (a). We also re-arrange the XD-GRASP recovered frames to form a temporal profile, in the top-row. Specifically, we constructed a time series by picking the XD-GRASP frames corresponding to the identified cardiac and respiratory phases. We observe that some of the cardiac/respiratory phases are not well sampled in XD-GRASP due to variable breathing cycles, resulting in blurring and aliasing artifacts. See phases outlined by green boxes. By contrast, our soft-binning strategy exploits the similarity between the phases along the time series to reduce these artifacts. The weight patterns for two frames indicated by the yellow and red arrows are shown in the top row. We note that the weights are high whenever the frames are similar to the chosen frame; the algorithm combines the information in these similar frames to obtain high-resolution reconstructions.

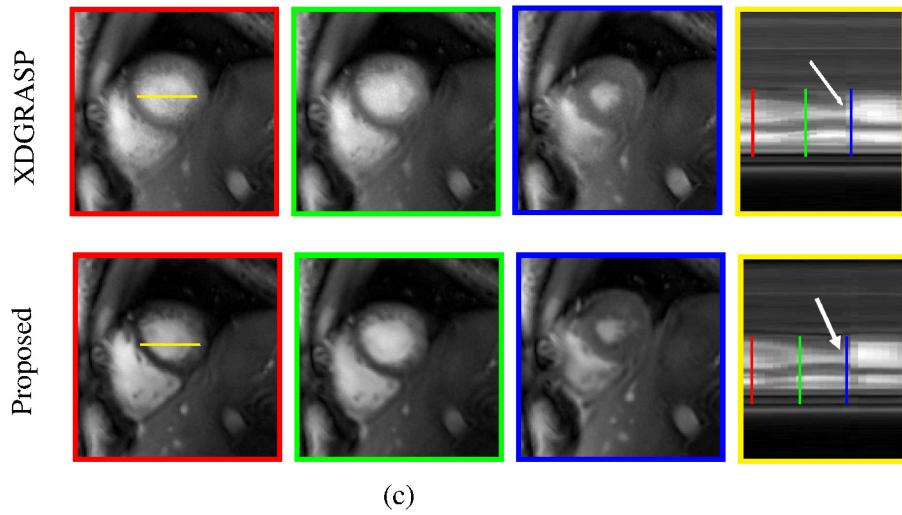
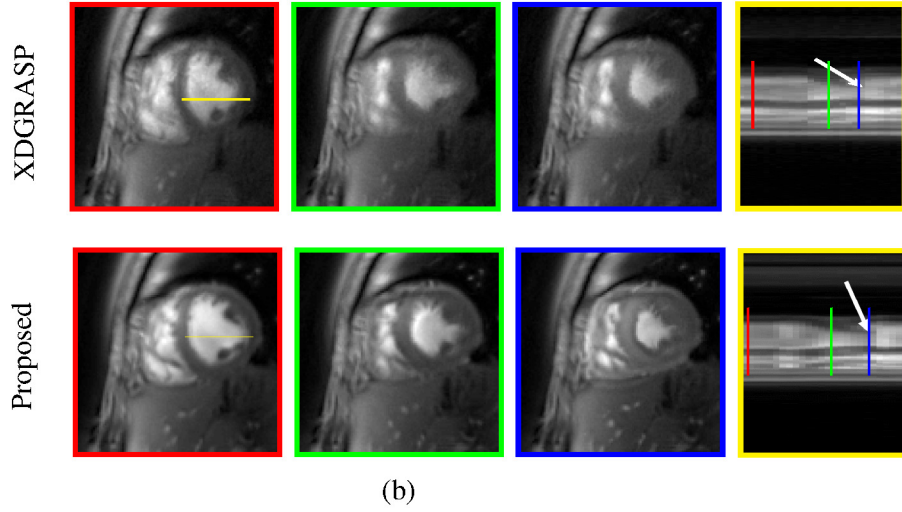


Figure 6: Comparison of the proposed scheme against XD-GRASP. We show the frames from our dataset that closely match the ones recovered using XD-GRASP. Note that we do not expect a perfect match in anatomy since XD-GRASP performs an averaging of data within respiratory bins. Three spatial frames are shown, picked from the locations indicated in the temporal profiles with red, green blue lines. The proposed method has less blurring as compared to the XDGRASP method, as the XDGRASP method is averaging the data within a respiratory state. White arrows are used to show the end systole phase, which is well captured by both methods.